Continuum Mech. Thermodyn. (2018) 30:53–68
https://doi.org/10.1007/s00161-017-0582-x

ORIGINAL ARTICLE

F. Welsch · J. Ullrich · H. Ossmer · M. Schmidt ·
M. Kohl · C. Chluba · E. Quandt · A. Schütze · S. Seelecke

Numerical simulation and experimental investigation of the elastocaloric cooling effect in sputter-deposited TiNiCuCo thin films

Received: 2 December 2016 / Accepted: 13 June 2017 / Published online: 26 June 2017

Abstract The exploitation of the elastocaloric effect in superelastic shape memory alloys (SMA) for cooling applications shows a promising energy efficiency potential but requires a better understanding of the non-homogeneous martensitic phase transformation. Temperature profiles on sputter-deposited superelastic $Ti_{55.2}Ni_{29.3}Cu_{12.7}Co_{2.8}$ shape memory alloy thin films show localized release and absorption of heat during phase transformation induced by tensile deformation with a strong rate dependence. In this paper, a model for the simulation of the thermo-mechanically coupled transformation behavior of superelastic SMA is proposed and its capability to reproduce the mechanical and thermal responses observed during experiments is shown. The procedure for experiment and simulation is designed such that a significant temperature change from the initial temperature is obtained to allow potential cooling applications. The simulation of non-local effects is enabled by the use of a model based on the one-dimensional Müller–Achenbach–Seelecke model, extended by 3D mechanisms such as lateral contraction and by non-local interaction, leading to localization effects. It is implemented into the finite element software COMSOL Multiphysics, and comparisons of numerical and experimental results show that the model is capable of reproducing the localized transformation behavior with the same strain rate dependency. Additionally to the thermal and the mechanical behavior, the quantitative prediction of cooling performance with the presented model is shown.

Communicated by Andreas Öchsner.

F. Welsch (✉) · J. Ullrich · M. Schmidt · S. Seelecke
Intelligent Material Systems Lab, Saarland University, Gewerbepark Eschberger Weg 46, Building 9,
66121 Saarbruecken, Germany
E-mail: felix.welsch@imsl.uni-saarland.de

S. Seelecke
E-mail: stefan.seelecke@imsl.uni-saarland.de

A. Schütze
Lab for Measurement Technology, Saarland University, Saarbruecken, Germany
E-mail: schuetze@lmt.uni-saarland.de

H. Ossmer · M. Kohl
Institute of Microstructure Technology, Karlsruhe Institute of Technology, Karlsruhe, Germany

M. Kohl
E-mail: manfred.kohl@kit.edu

C. Chluba · E. Quandt
Institute for Material Science, University of Kiel, Kiel, Germany

E. Quandt
E-mail: eq@tf.uni-kiel.de

Keywords Elastocaloric cooling · Shape memory alloy · TiNiCuCo thin film · Thermo-mechanical coupling · Rate dependence · Localization · Propagating transformation fronts · Finite element analysis · Phase transformation · Thermodynamics

1 Introduction

Superelastic shape memory alloys (SMA) gained attention in research for solid-state cooling because of the elastocaloric effect [1]. Release and absorption of latent heat associated with stress-induced martensitic phase transformation cause considerable temperature changes during this thermo-mechanically coupled process, which can be used to transport heat [2,3]. One aspect that motivates the replacement of traditional fluid-based cooling cycles by alternatives is the need to eliminate the use of ozone-depleting refrigerants. Another aspect is the higher energy efficiency potential of cooling cycles based on the elastocaloric effect [4].

This effect has been investigated in bulk material during tensile [5,6] and bending deformation [7], but also in thin films under tension [8–10]. Ferroelastic cooling using such thin films could be applied in microscale devices, where the elastocaloric effect may be used for cooling in biomedical or lab-on-a-chip applications [11,12].

Recent research on Ti-rich TiNiCu and TiNiCuCo shape memory alloys [13,14] shows their outstanding resilience against fatigue which makes them a promising material for applications where it is necessary that the material can sustain a high number of load cycles. As shown in [15], the addition of cobalt lowers the transformation temperatures allowing their adjustment in order to obtain pseudoelasticity. Compared to binary NiTi, these alloys exhibit a smaller hysteresis and a substantially smaller transformation strain. This may be a drawback in some applications, but for the use in a ferroelastic cooling device this is a favorable property because it reduces the mechanical work input required to perform the stress-induced martensitic phase transformation [10,13].

Several models based on free energy principles have been proposed for the simulation of shape memory alloys [16–25]. Some of these models provide a physically motivated description of the thermo-mechanically coupled behavior of SMA material, while others assume an isothermal case.

When an SMA sample is subjected to a tensile deformation, a localized phase transformation with a strong strain rate dependence can be observed [26]. The stress–strain behavior of SMA is directly influenced by the strain rate due to the distinct thermo-mechanical coupling: higher strain rate means more exothermic (endothermic) phase transformation per time and consequently higher (lower) temperature leading to higher (lower) transition stress and generating more phase fronts. So far, few approaches have been developed to model the localized behavior for simulation with finite element software [27–31]. These have in common that they introduce models using a localization effect and a non-local extension in order to account for localized phase transformations and continuous transitions between austenitic and martensitic regions. Typically, the localization effect is generated by a local softening behavior during phase transformation. Various approaches for the non-local extension exist and vary from strain gradient methods [27] over phase gradient energy [29,31] to Green's functions [28].

This paper presents numerical simulations of the thermo-mechanically coupled behavior of TiNiCuCo thin-film samples and compares them to experimental measurements. The model we are using is an extended version of the one-dimensional Müller–Achenbach–Seelecke (MAS) model [21,23]. This model has been used for the thermo-mechanically coupled simulation in finite element software of actuator wires [32], superelastic wires [33] and superelastic beams [7,34]. In bending problems, the deformation case already induces a localized phase transformation. In models simulating SMA wires though, the experimentally observed localized transformation has been neglected.

In the present case, we focus on reproducing the localized behavior and extend the MAS model by a localization effect, resulting from the combined consideration of lateral contraction and a transformation softening behavior. The non-local extension consists of the scaled contribution of the second spatial derivative of the martensitic phase field to the kinetic equations of phase transformation [9].

As samples with a very thin geometry are considered in the present study, temperature variations across the sample thickness are negligible. The slight variation of temperature profiles in lateral direction due to the inclination angle of strain bands is also neglected because important measures like the number of strain bands and their propagation velocity are independent of the lateral position. Therefore, we treat the tensile deformation of the film as a one-dimensional problem and compare one-dimensional simulation results to temperature data from measurements collected along the centerline on the film surface.

By comparing simulation results to experimental measurements, we show that our model captures the distinctive characteristics observed in the experiment. These include the thermal dependence of transformation stress, the rate dependence of the phase front localization, incomplete phase transformations during loading and unloading as well as continued transformations during holding phases. Furthermore, the model recreates the mechanical work input as well as the exchanged thermal work output which allows calculation of the coefficient of performance (COP), an important reference value for caloric processes.

2 Experiment

2.1 Setup

Uniaxial tensile tests are performed in an experimental setup as sketched in Fig. 1. Film samples are attached to alumina plates on both ends with two-component adhesive, which are then mounted in the sample holder of a Zwick tensile test machine. Thus, stress peaks at the clamping are avoided. During the experiment, the lower end of the sample is held in constant position, while the upper end is displaced by a ball screw drive. Forces are measured by a load sensor with a resolution of 0.25 N. An infrared camera (FLIR A655sc) with spatial and temporal resolution of 25 µm and 10 ms, respectively, is used to monitor the temperature distribution of the sample. The factory calibration of the camera with macro lens allows a temperature range of −40 °C to +150 °C. To achieve a higher emissivity of the metallic specimen surface, the sample is thin coated with a graphite lacquer (Graphit 33). In preparation of the experiment, the infrared measurement on the graphite coating showed good agreement with pointwise direct temperature measurements.

For the experiments, we used a sputter-deposited $Ti_{55.2}Ni_{29.3}Cu_{12.7}Co_{2.8}$ thin film with the dimension 15 mm × 1.75 mm × 18 µm. TiNiCu-based films with Ti overhead exhibit almost no fatigue behavior even after millions of load cycles due to Ti_2Cu precipitations [14]. The differential scanning calorimetry (DSC) measurement (NETZSCH Phoenix) of the sample with a temperature rate of 10 K/min is shown in Fig. 2. Apparent double peaks are due to the heterogeneity of the sample material. From this measurement, the latent heat associated with the phase transformation has been determined to be 13.7 J/g. However, the latent heat accessible in the tensile test experiments is often smaller than that observed in DSC [9]. Therefore, we consider a lower latent heat for our simulations as will be discussed later in this paper. The specific heat capacity c of the sample as measured by DSC is 420 J/kg/K. We assume the same value for both martensite and austenite, which is also supported by DSC results [10].

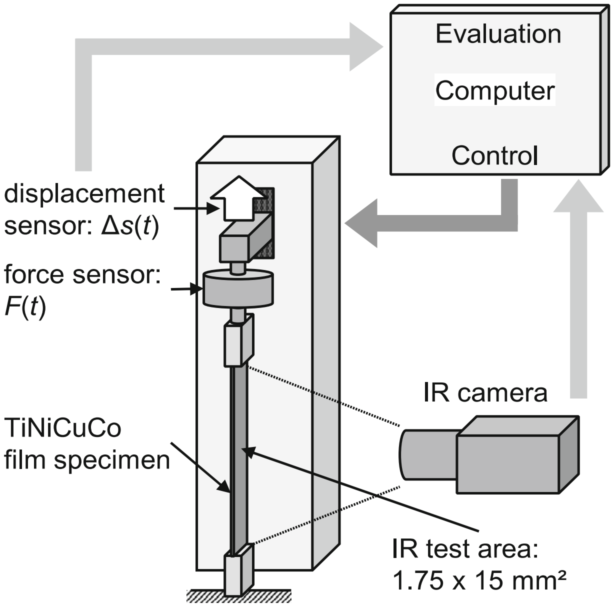

Fig. 1 Experimental setup for uniaxial tensile tests with IR thermography

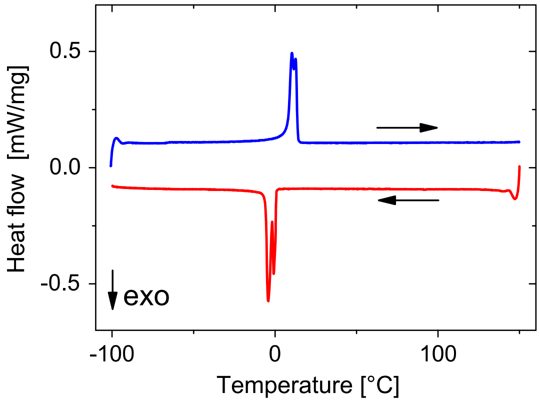

Fig. 2 DSC measurement of the TiNiCuCo sample

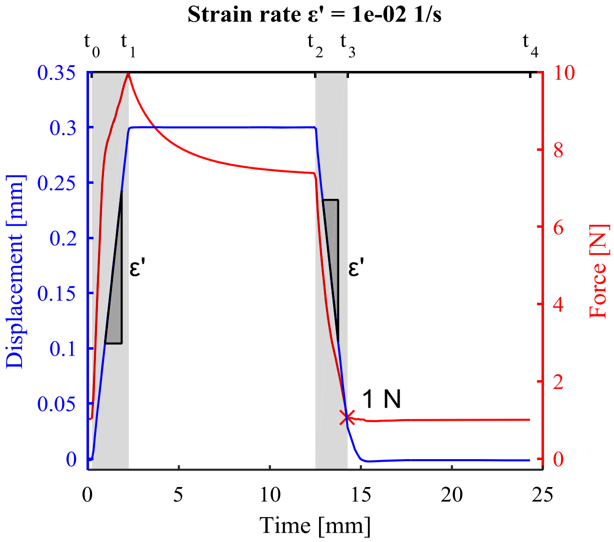

Fig. 3 Example load path for strain rates $\varepsilon' = 10^{-2}\,\mathrm{s}^{-1}$

2.2 Procedure

Figure 3 illustrates the load path used in the experiments: first, the film is preloaded such that a small force of 1.0 N is applied, which corresponds to a nominal stress of 32 MPa and a nominal strain of 8.0×10^{-4}. Then at t_0, the linear actuator controls the displacement of the substrate such that the film is stretched with a specific strain rate to an additional strain of 2% at t_1. Subsequently, this state is held for 10 s before unloading begins at t_2 with the same strain rate as for loading. During loading, latent heat is released due to the martensitic phase transformation, which heats the sample. The holding period duration is chosen such that the sample reaches ambient temperature again. This is crucial for maximizing the temperature difference (minimizing the temperature) obtained during unloading, which is an important parameter for cooling devices. When during unloading the axial load reaches 1 N again at t_3, the linear actuator's mode is changed back to force controlled in order to keep the load constant, which keeps the film under tensile load and avoids buckling. This period also lasts 10 s up to t_4 allowing the sample to again return to ambient temperature.

2.3 Results

In this section, we show the exemplary experimental results for strain rates of $d\varepsilon/dt = \varepsilon' = 10^{-3} \ldots 10^{-1}\,\mathrm{s}^{-1}$. More detailed results with time resolved quantities are arranged for comparison in a later section together with simulation results.

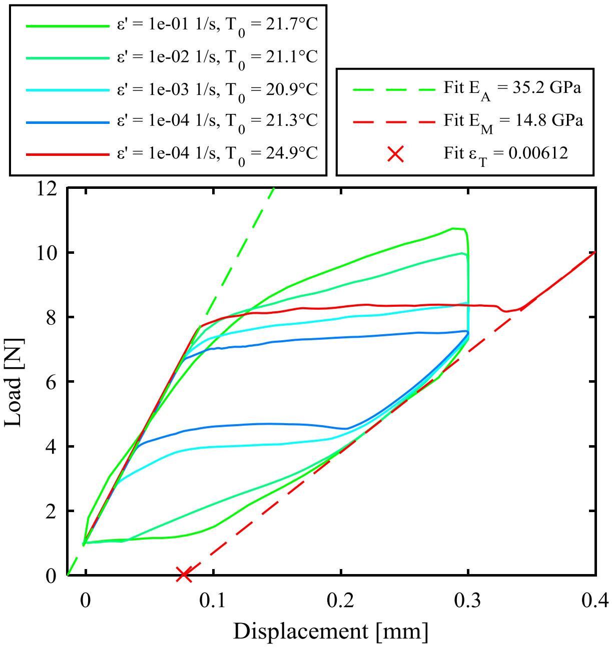

Fig. 4 Experimental load–displacement diagrams for different strain rates $\varepsilon' = 10^{-3} \dots 10^{-1}\,\mathrm{s}^{-1}$ and fitted Young's moduli of austenite E_A and martensite E_M as well as transformation strain ε_T

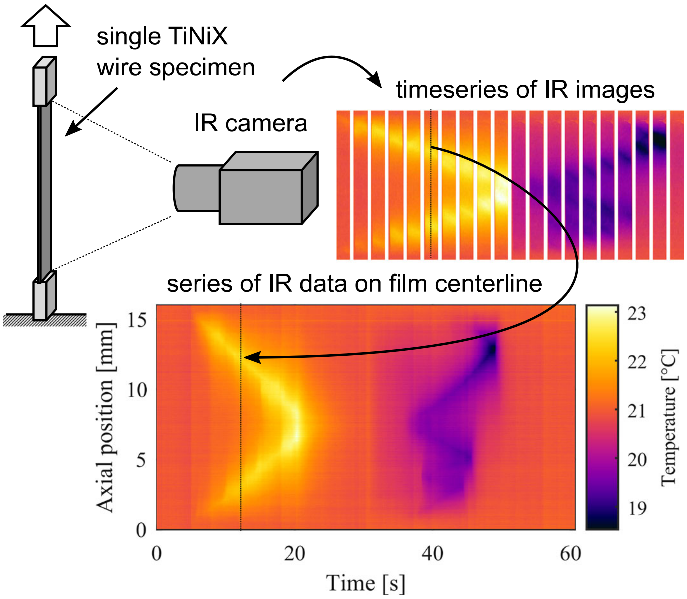

Fig. 5 Spatiotemporal representation of the thermal evolution at the *center line* of the film surface for strain rate $\varepsilon' = 10^{-3}\,\mathrm{s}^{-1}$

Figure 4 illustrates load as a function of displacement where the zero displacement position has been shifted to the preloaded initial state. The ambient air temperature near the sample varies slightly between experiments with different strain rates as shown in the legend. The data of the experiment with the highest strain rate contain artefacts due to sampling rate limitations of the tensile test machine resulting in deviations at the elastic austenitic branch during loading and a curved representation of transformation start. The time series of IR-images in Fig. 5 shows the appearance of temperature bands moving over time indicating the presence of propagating phase fronts. The load–displacement relationship reveals that the transformation stress increases during phase transformation due to the thermo-mechanically coupled material behavior. During the holding periods after loading with higher strain rates, a drop in force is observed. This indicates that the phase transformation was not completed during loading because a decreasing temperature also reduces the transformation stress allowing further material to transform. This ongoing transformation leads to further local expansion of the material resulting in the force relaxation. If the transformation is already complete during loading as for the lower strain rates, no force reduction is observed during the holding phase.

The different start behavior of the transformations during loading and unloading in the IR-images is another indicator for an incomplete transformation. During loading, the phase transformation starts at both ends of the sample. During unloading, however, the transformation starts near the center where the temperature peaks joined before during loading. This indicates that the apparent meeting of the phase fronts did not result in a full transformation. Instead, an un- or less transformed region remains, where nucleation is preferred during unloading.

For further analysis, we neglect variations over the width and thickness of the sample as motivated above. For better visualization and easier comparison with simulation results, the thermal evolution along the centerline of the film is arranged in a spatiotemporal representation as shown in Fig. 5.

2.4 Parameter identification

For modeling the behavior of the sample, the relevant mechanical and thermal parameters of the material and the setup must be identified.

As shown in Fig. 4, the Young's modulus of austenite E_A is directly derived from the experimental load-displacement data taking the specimen geometry into account. For identification of martensite modulus E_M and transformation strain ε_T, the assumption of a fully transformed sample is necessary. This is satisfied by a final quasi-isothermal tensile test with a strain rate of $\varepsilon = 10^{-4}\,\mathrm{s}^{-1}$ until the linear elastic martensite branch is reached, pictured as red line in Fig. 4, which reassures the derived mechanical parameters.

Another important parameter describing the thermo-mechanical coupling is the temperature dependence of transformation stresses for forward and reverse transformation (Clausius–Clapeyron coefficients). For binary NiTi, these values are typically around $7\,\mathrm{MPa/K}$ as determined by isothermal tensile tests at different temperatures. However, due to the space-resolved temperature data a direct identification of these parameters for the new TiNiCuCo material is possible from the experiments presented above. Since the transformation stress directly depends on the temperature at the transforming region (phase front) and all other regions do not influence the axial force because they are not yet or already fully transformed, the transformation stress correlates with the phase front temperature. Tracking of the phase fronts is achieved by searching local temperature maxima during loading and temperature minima during unloading. Figure 6 presents the correlation of axial tensile

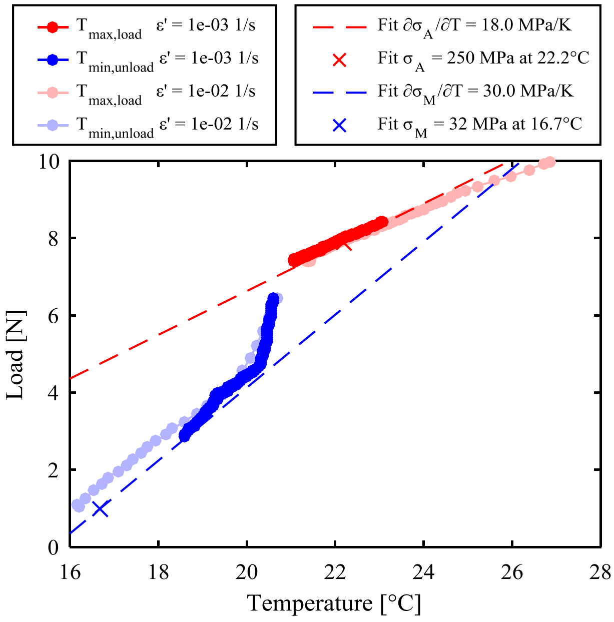

Fig. 6 Measured tensile load and observed phase front temperatures to derive the temperature dependence of the transformation stresses and stresses at reference temperatures

force and phase front temperature: During loading (red dots), the phase front temperature rises from ambient to a strain rate-dependent maximum. The axial force equivalent to the forward transformation stress follows the increasing temperature quite linearly with a slope of 30 MPa/K. During unloading after the holding period, the phase front temperature (blue dots) starts again at ambient and then drops to a rate-dependent minimum. After an initial bend, the slope of the reverse transformation stress settles to 18 MPa/K. These unequal and high values are unusual compared to binary NiTi; however, they are confirmed by the simulation results discussed later.

The influence of the environment on the sample is represented by the surrounding air temperature T_0 and the convective heat exchange coefficient h. Since the sample had sufficient time to equalize any temperature differences before the experiment, the air temperature is derived directly from the average sample temperature at the beginning.

The convective heat exchange coefficient is determined from the temperature relaxation of the sample during holding phases. To allow a better comparison between experiments with different strain rates and therefore differing start temperature T_s, a normalized temperature $\tilde{T}$ is introduced, as shown in Eq. (1). Under the assumption of a homogeneous temperature distribution, negligible influence of the clamping and no generation or absorption of latent heats, the evolution of temperature is governed by an exponential decay dependent on the heat exchange coefficient h and other already known material parameters:

$$\tilde{T}\,(t) = \frac{T\,(t) - T_0}{T_\mathrm{s} - T_0} \approx \exp\left(-\frac{h \cdot A}{\varrho \cdot c \cdot V} \cdot t\right) \tag{1}$$

These assumptions are satisfied fairly well for the center region of the sample, where the distance to the clamping is sufficiently large to neglect their influence and the joining phase fronts create an almost homogeneous temperature field.

Latent heats released or absorbed due to stress relaxation during holding phases contribute to the internal energy and slow down the decay in normalized temperature. When the relaxation-induced transformation completes, the temperature is controlled exclusively by Eq. (1) leading to a faster temperature drop. Thus, the presence of a kink to higher slope in the cooling curve indicates the end and magnitude of the relaxation process.

Figure 7 displays the normalized temperature decay during holding after loading and unloading with different strain rates. Since the curves show no distinctive bend, a negligible influence of relaxation processes is assumed. The resulting estimation for the heat exchange coefficient $h = 18\,\mathrm{W/K/m^2}$ is plotted for comparison in Fig. 7.

All above discussed and derived parameters are summarized in Table 1.

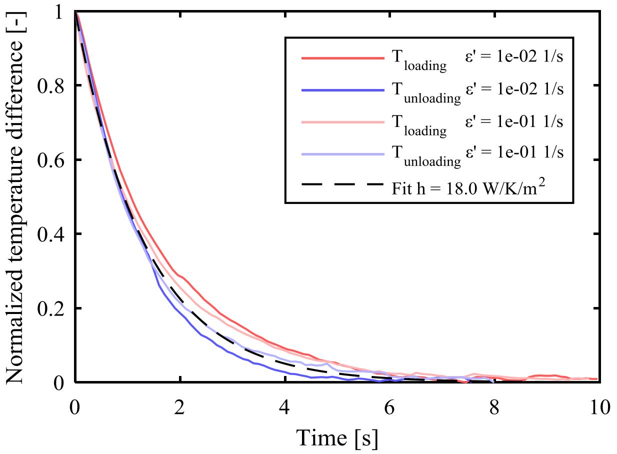

Fig. 7 Normalized experimental temperature decay during holding phases after loading and unloading for identification of the convective heat transfer coefficient *h*

Table 1 List of model parameters

Parameter	Value	Unit	Description
L	15	mm	Sample length
D	18	µm	Sample thickness
W	1.75	mm	Sample width
E_{A}	35.2	GPa	Young's modulus of austenite
E_{M}	14.8	GPa	Young's modulus of martensite
ε_{T}	0.00612	–	Transformation strain
ν_{e}	0.33	–	Poisson's ratio of elastic strain
ν_{t}	0.5	–	Poisson's ratio of transformation strain
ϱ	6450	$\mathrm{kg/m^3}$	Mass density
c	420	J/kg/K	Specific heat capacity
κ_{A}	9	W/m/K	Thermal conductivity austenite
κ_{M}	4.5	W/m/K	Thermal conductivity martensite
H	5	J/g	Latent heat
h	18	$\mathrm{W/m^2/K}$	Convection coefficient
T_0	~ 21	°C	Environment temperature
$\sigma_{\mathrm{A}}(T_{\mathrm{A}})$	250	MPa	Austenite transformation stress at T_{A}
T_{A}	22.2	°C	Reference temperature
$\partial\sigma_{\mathrm{A}}/\partial T$	18	MPa/K	Temperature dependence of transformation stress
$\sigma_{\mathrm{M}}(T_{\mathrm{M}})$	32	MPa	Martensite transformation stress at T_{M}
T_{M}	16.7	°C	Reference temperature
$\partial\sigma_{\mathrm{M}}/\partial T$	30	MPa/K	Temperature dependence of transformation stress
$\beta_{\mathrm{A}},\ \beta_{\mathrm{M}}$	24	MPa	Phase dependence of transformation stress
η	12×10^{-8}	$\mathrm{m^2/s}$	Coefficient for non-local phase field contribution
V_{LE}	5×10^{-20}	$\mathrm{m^3}$	Volume element size
τ_{x}	0.001	s	Time constant of phase transition

2.5 Cooling performance

To evaluate the cooling efficiency of the emulated elastocaloric cooling process with heat sink and source at ambient temperature T_0, the coefficient of performance (COP) is calculated for each experiment.

The COP is defined as the ratio of absorbed thermal energy at the heat source and dissipated mechanical work during one cycle:

$$\mathrm{COP} = \frac{Q_{\mathrm{th,absorbed}}}{W_{\mathrm{me,dissipated}}} \tag{2}$$

The stored mechanical work W_{me} in the sample is expressed as the time integral of the mechanical power input P at clamping:

$$W_{\mathrm{me}}(t) = \int_0^t P(\tau)\,\mathrm{d}\tau \tag{3}$$

$$P(t) = F(t) \cdot v(t) = \sigma(t) \cdot A(t) \cdot \frac{\mathrm{d}u}{\mathrm{d}t}(t) \tag{4}$$

Due to the hysteresis in the stress-strain behavior of the material, not all mechanical energy introduced during loading is recovered during unloading. The dissipated mechanical work is the difference in mechanical work between start and end of a cycle (cp. Sect. 2.2):

$$W_{\mathrm{me,dissipated}} = W_{\mathrm{me}}(t_4) - W_{\mathrm{me}}(t_0) \tag{5}$$

The thermal energy Q_{th} exchanged with the environment is defined by the time integral of the heat flux Q'' through the surface area $S = 2 \cdot (W + D) \cdot L$ of the specimen. The heat flux density is determined in every surface point x of the surface S by the local temperature difference to the ambient and the heat transfer coefficient h:

$$Q_{\mathrm{th}}(t) = \int_0^t \dot{Q}(\tau)\ \mathrm{d}\tau \tag{6}$$

$$\dot{Q}(t) = -\oiint h \cdot (T(x,t) - T_0)\ \mathrm{d}S \tag{7}$$

The heat absorbed from the heat source during unloading and the subsequent holding phase is the difference in thermal energy between start and end of this part in the cycle:

$$Q_{\mathrm{th,absorbed}} = Q_{\mathrm{th}}(t_4) - Q_{\mathrm{th}}(t_2) \tag{8}$$

To evaluate the predictive power of the described SMA model for cooling efficiency, these calculations are applied to both the experimental data and the simulation results.

3 Modeling and simulation

3.1 SMA model equations

For the simulation of the localized transformation behavior of superelastic SMA material during tensile deformation, we use a model based on the MAS model [21,23]. This model assumes homogeneous material properties and considers global phase fractions for austenite x_A, a tensile martensite variant x_+ and a compressive martensite variant x_-. The transformation rates between these variants are described by differential equations derived from statistical thermodynamics and the algebraic relation $x_A + x_+ + x_- = 1$. In the present case with only tensile stress, the occurrence of a compressive martensite variant is excluded by procedure design and the corresponding phase fraction x_- remains at zero and is therefore omitted.

Here, we use a modified version of this model in order to account for localized effects observed in thermography. Therefore, phase fractions are considered as local quantities $x_+(x,t)$ and are position and time dependent, just like the displacement field $u(x,t)$ and the temperature field $T(x,t)$, following [32]. The essential modifications of the model account for localization combined with a non-local extension. These extensions enable us to reproduce the phenomenon of traveling temperature peaks caused by transformations at multiple phase fronts. Localization in our model is induced by two effects: lateral contraction and a material softening during isothermal phase transformation.

The global mechanical behavior of the model is governed by the one-dimensional stationary momentum balance in loading direction:

$$\frac{\partial(\sigma \cdot A)}{\partial x} = 0 \tag{9}$$

The local stress σ is described by a constitutive relation, which accounts for the phase fraction-dependent stress–strain behavior:

$$\sigma = \frac{\varepsilon - \varepsilon_{\mathrm{T}} \cdot x_+}{\frac{x_+}{E_{\mathrm{M}}} + \frac{1-x_+}{E_{\mathrm{A}}}} \tag{10}$$

Local strain ε is determined from the displacement field:

$$\varepsilon = \frac{\partial u}{\partial x} \tag{11}$$

In the stress–strain relation (10), thermal expansion is neglected as it is much smaller than the strain induced by the phase transformation.

In the expression for the non-constant cross-sectional area

$$A = W \cdot D \cdot (1 - \nu_{\mathrm{e}} \cdot \varepsilon_{\mathrm{e}} - \nu_{\mathrm{t}} \cdot \varepsilon_{\mathrm{t}})^2, \tag{12}$$

we consider an isochoric contribution to the lateral contraction induced by a transformation strain

$$\varepsilon_{\mathrm{t}} = \varepsilon_{\mathrm{T}} \cdot x_+ \tag{13}$$

and a contribution induced by elastic strain

$$\varepsilon_{\mathrm{e}} = \varepsilon - \varepsilon_{\mathrm{t}}. \tag{14}$$

This induces a reduction in the cross section with increasing strain, which in turn leads to locally increased stress.

Additionally, compared to the original model, we modify the transformation stresses σ_{A} and σ_{M} to be not only temperature but also phase dependent:

$$\sigma_{\mathrm{A}} = \sigma_{\mathrm{A}}\left(T_{\mathrm{A}}\right) + \frac{\partial \sigma_{\mathrm{A}}}{\partial T} \cdot \left(T - T_{\mathrm{A}}\right) + \beta_{\mathrm{A}} \cdot \left(1 - x_{+}\right), \tag{15}$$

$$\sigma_{\mathrm{M}} = \sigma_{\mathrm{M}}\left(T_{\mathrm{M}}\right) + \frac{\partial \sigma_{\mathrm{M}}}{\partial T} \cdot \left(T - T_{\mathrm{M}}\right) - \beta_{\mathrm{M}} \cdot x_{+} \tag{16}$$

The phase fraction dependence of the transformation stresses as used in Eqs. (15) and (16) follows the motivation of a coherency energy contribution in [35], similar to the interaction energy in [27], leading to a softening during martensite generation at isothermal conditions.

The temperature and phase fraction-dependent transformation stress contribute to the construction of a multi-parabolic free energy landscape, which determines transition probabilities

$$p^{\alpha\beta} = \frac{1}{\tau_{\mathrm{x}}} \cdot \exp\left(-\frac{\Delta g_{\alpha\beta}\left(\sigma, T\right) \cdot V_{\mathrm{LE}}}{k_{\mathrm{B}} \cdot T}\right) \tag{17}$$

describing the probability for a representative layer volume to overcome an energy barrier between phases [23]. These transition probabilities introduce a thermo-mechanical coupling due to their dependence on the stress and temperature state and determine the transition rate in the kinetic equations for phase transformation:

$$\frac{\partial x_{+}}{\partial t} - \eta \cdot \frac{\partial^{2} x_{+}}{\partial x^{2}} = -x_{+} \cdot p^{+\mathrm{A}} + \left(1 - x_{+}\right) \cdot p^{\mathrm{A}+} \tag{18}$$

Compared to the original model, Eq. (18) is modified in order to enforce continuity between phases by adding the contribution of the second derivative of the respective phase field scaled by a factor η as non-local extension. Without this modification, transitions between phases would be discontinuous. Synchrotron X-ray diffraction performed on a partially transformed NiTi wire in [36] shows that a transition zone between a region in austenite phase and a region in martensite phase exists.

The evolution of the temperature field is determined by the one-dimensional internal energy balance:

$$\varrho c \frac{\partial T}{\partial t} - \frac{\partial}{\partial x}\left(\kappa \frac{\partial T}{\partial x}\right) = -h \cdot \left(T - T_{0}\right) + H \varrho \frac{\partial x_{+}}{\partial t} \tag{19}$$

Here, an effective thermal conductivity is used depending on the phase fractions:

$$\kappa = x_{+} \cdot \kappa_{\mathrm{M}} + \left(1 - x_{+}\right) \cdot \kappa_{\mathrm{A}} \tag{20}$$

Local heat source contributions include the release or absorption of latent heats, depending on the transformation direction and rate, on the one hand, and convective heat exchange with the environment, on the other hand.

The model is implemented into the commercially available finite element software COMSOL Multiphysics [37]. This software allows simulating custom partial differential equation (PDE) systems on a one-dimensional geometry. Our PDE system consisting of Eqs. (9), (18) and (19) is implemented such that the software solves for the displacement $u\left(x, t\right)$, phase fraction $x_{+}\left(x, t\right)$ and temperature $T\left(x, t\right)$ fields.

3.2 Boundary conditions

The clamps at both ends of the film are very similar; therefore, equal boundary conditions for temperature and external load are considered at both ends. Using this symmetry, only one half of the film length is simulated in the finite element software and symmetric phase transformation with respect to the longitudinal sample center is assumed. For the mechanical boundary conditions, this means that while one end of the one-dimensional geometry remains fixed (21), the displacement $\bar{u}\left(t\right)$ of the other end corresponding to the center of the sample is prescribed (22).

$$u\left(x = 0, t\right) = 0 \tag{21}$$

$$u\left(x = \frac{L}{2}, t\right) = \bar{u}\left(t\right) \tag{22}$$

For the holding phase after unloading, the boundary condition (22) is replaced by a constant load boundary condition (23):

$$F\left(x=\frac{L}{2},t\right)=1\,\mathrm{N} \tag{23}$$

As the ends of the film are attached to substrates, we assume that the temperature remains at ambient temperature due to the high heat capacity of the substrate with respect to the film (24). Following the symmetry assumption, the temperature gradient in the middle of the film is zero (25):

$$T\left(x=0,t\right)=T_0 \tag{24}$$

$$\frac{\partial T}{\partial x}\left(x=\frac{L}{2},t\right)=0 \tag{25}$$

For the phase fields, homogeneous Neumann boundary conditions are assumed:

$$\frac{\partial x_+}{\partial x}\left(x=0,t\right)=\frac{\partial x_+}{\partial x}\left(x=\frac{L}{2},t\right)=0 \tag{26}$$

3.3 Procedure

The mechanical boundary conditions are applied in a sequence corresponding to the experimental procedure (cp. Sect. 2.2). Unlike the experiment, we start the simulation from zero load. As the material behavior under the low preload is purely elastic, the transformation behavior remains unchanged. The time axis of the simulation is shifted to allow direct comparison with experimental results. An event detection provided by the finite element software is used during unloading to determine the precise moment when a load of 1 N is reached again. This interrupts the simulation and changes the mechanical boundary condition from displacement controlled (22) to force controlled (23) allowing further axial contraction of the film induced by continuing transformation if the phase transformation back to austenite was not already completed during unloading.

For the simulation of the described SMA model in the finite element software, the singular set of model parameters in Table 1 is used. These parameters were identified from the experimentally observed mechanical and thermal behavior as presented above. The value for the latent heat is significantly lower than that determined by DSC measurement. This value was selected manually to match temperature peak values determined in the simulation to the temperature values observed in experiments at high strain rates in the adiabatic limit. At such high strain rates, the temperature evolution in the sample depends only on the percentage of transforming material, the latent heat and specific heat capacity since thermal exchange with environment is negligible due to the tiny loading time span. The value of the specific heat capacity was determined with reasonable certainty by DSC; furthermore, the amount of transforming material is defined by the applied strain and the temperature during loading. Consequentially the latent heat is the remaining degree of freedom to adjust the temperature evolution in the adiabatic limit. A value of $H = 5\,\mathrm{J/g}$ generates a matching mean temperature evolution during loading with the highest strain rate. In the experiments with decreasing strain rates, the thermal convection gains increasing influence on the thermal evolution lowering the peak temperatures. The adequate prediction for the mean temperature during both lower-strain-rate experiments gives confirmation for the chosen value (Fig. 8 third row). We assume that the difference in latent heat in temperature (DSC) and stress-induced (tensile experiment) transformation corresponds to a locally incomplete phase transformation as previously observed in [38–40].

Since no directly measured values for the thermal conductivity of austenitic and martensitic phase of the new TiNiCuCo material are available, these parameters were chosen to match the width and height of temperature peaks during localization. When loading with the slowest strain rate, only two traveling temperature peaks were observed. The width and height of these peaks are defined by the size of the transforming region, the thermal conductivity and available time for thermal diffusion corresponding to strain rate. The width of the transforming region is not directly measurable in this setup but is assumed to be in the order of the material thickness resulting in few individual pixels in the infrared image. Consequentially, the width of the temperature peak is mainly defined by the thermal conductivity. Starting with typically values for binary NiTi as $\kappa_\mathrm{A} = 18\,\mathrm{W/m/K}$ and $\kappa_\mathrm{M} = 9\,\mathrm{W/m/K}$, the thermal conductivities were subsequently reduced while preserving their ratio until an appropriate temperature distribution at the propagating phase fronts was observed in the simulation of the slowest strain rate. The size of the temperature peaks also affects the distance between propagating phase

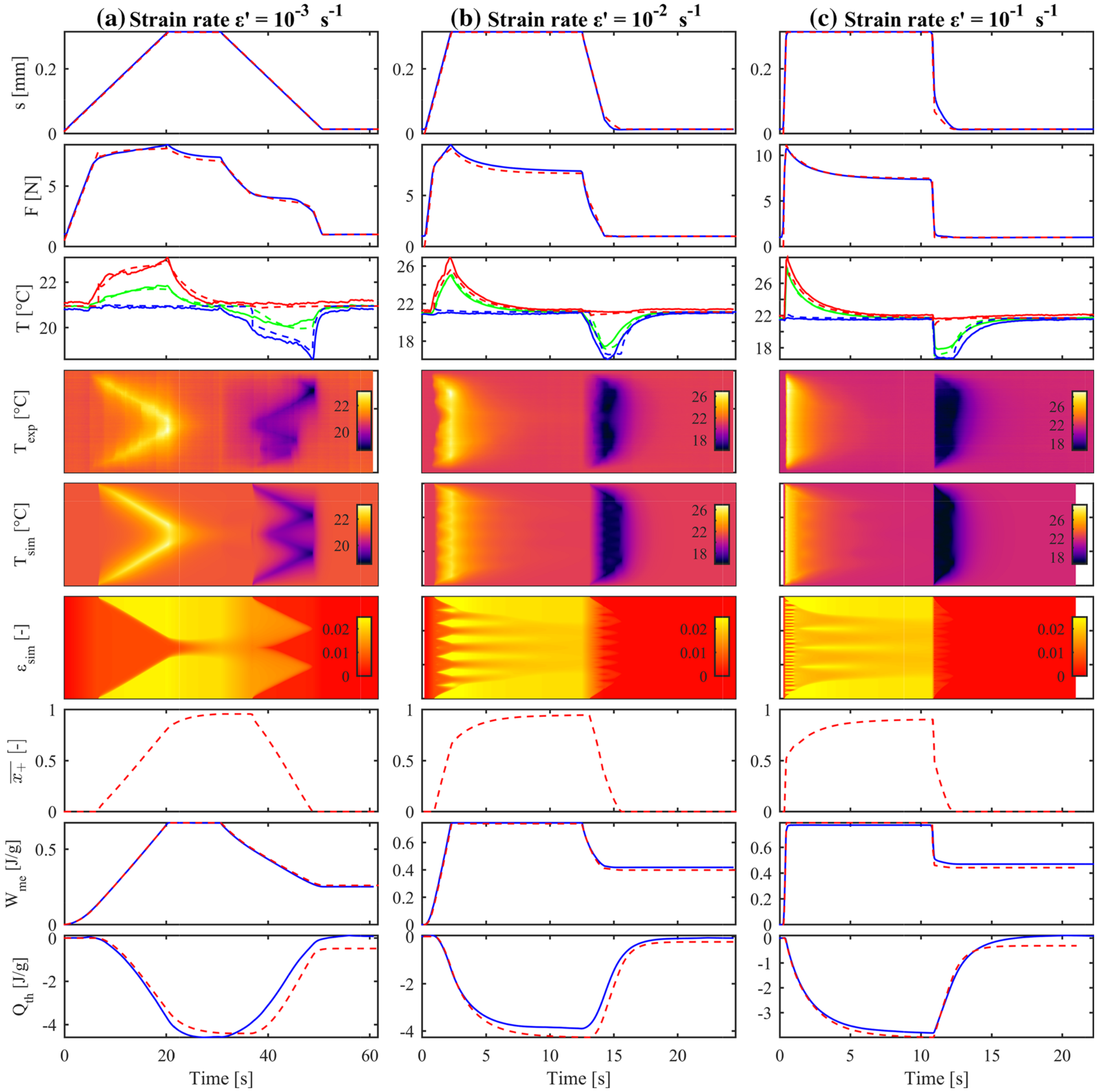

Fig. 8 Comparison of experimental data (*solid lines*) and simulation (*dotted lines*) for displacement, axial load, minimal/average/maximal temperature of the whole sample, spatiotemporal temperature evolution, spatiotemporal strain evolution, global martensite fraction, specific mechanical work and thermal energy

fronts in the experiment with medium strain rate since the preheated material at the leading edge of the phase front is impeded to transform due to the now increased transformation stress. We assume to found reasonable values for the thermal conductivity since the fourth and fifth rows of Fig. 8 add confirmation by showing good agreement with the number and distance of phase fronts during loading and unloading.

3.4 Results and comparison to experimental observation

The first column of Fig. 8 and the load-displacement diagram in Fig. 9 show the comparison of our simulation to experimental data for a strain rate of $10^{-3}\,\mathrm{s}^{-1}$. The model not only captures the global load–displacement behavior, we also observe that during loading in both, experiment and simulation, the inhomogeneous transformation starts at the clamping due to the preferred local low temperature and produces two phase fronts traveling toward the center. Even though the temperature peaks join at the end of the loading phase, the simulated strain field $\varepsilon_{\mathrm{sim}}$ and the total amount of tensile martensite $\overline{x_+}$ show that the phase transformation is not

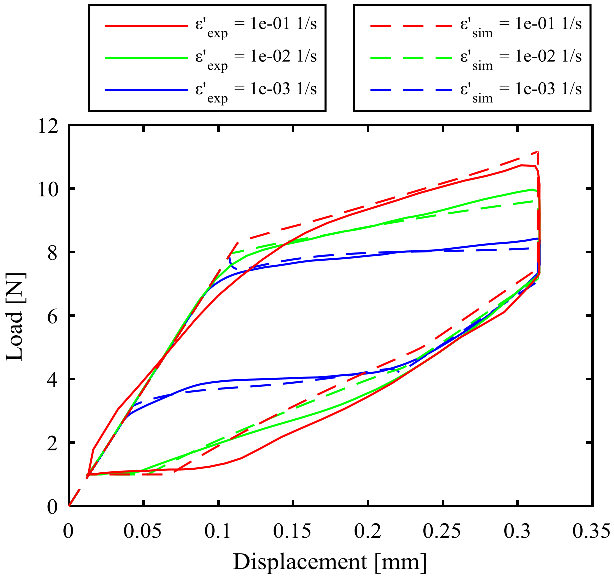

Fig. 9 Comparison of measured and simulated load–displacement diagrams for different strain rates $\varepsilon' = 10^{-3} \ldots 10^{-1}\,\mathrm{s}^{-1}$

complete. Looking at the evolution of the axial load during holding after loading, we notice a relaxation, which can only be caused by local strain changes. These are induced by continued transformation to martensite in the regions with previously incomplete transformation, as a lower stress is required for transformation when the sample cools down. As the strain in the transforming region increases, the strain in the fully transformed regions decreases elastically and a new force equilibrium is reached at a lower load level. This behavior is also revealed by the simulation as the total amount of martensite $\overline{x_+}$ keeps rising during the holding phase.

During unloading, the simulation reproduces the experimentally observed behavior that the reverse transformation starts in the region where the phase transformation was not complete. In addition, we observe more phase fronts than during loading in both experiment and simulation.

The thermal and mechanical behavior at higher strain rates (second and third column of Fig. 8) is distinctive in several ways. The increased slope in the load versus displacement diagrams of Fig. 9 and the higher stress level at the end of the loading phase is expected from the well-known thermo-mechanically coupled behavior of the SMA material.

The fact that the load relaxes to approximately the same value for all three investigated strain rates indicates that the duration of the holding phase of 10 s is sufficiently long. During unloading at higher strain rates, the phase transformation back to austenite is not complete over the whole sample before the load is held constant at 1 N. As shown by $\overline{x_+}$, the remaining martensite continues to transform during the holding phase as soon as the local temperature rises and the material's transformation stress reaches a sufficient level again. This means that the lowest temperature is reached at the end of the unloading phase. Therefore, even though the full amount of previously generated martensite transforms back to austenite during unloading and holding and contributes to heat absorption in general, only a reduced amount of martensite contributes to generating the temperature difference during unloading, since the reverse transformation is blocked by reaching the austenite finish temperature. This aspect will be of interest for the design of cooling devices, where both quantities contribute to the overall efficiency [4].

Another aspect captured by our model is the strain rate dependence of the number of phase fronts. We observe that a higher strain rate leads to the occurrence of a higher number of traveling temperature peaks, which indicate propagating phase fronts. New phase fronts appear when existing ones cannot travel sufficiently fast to transform enough material to account for the length change, which is imposed on the film by the boundary condition [26]. Local self-heating (self-cooling) at the phase fronts during transformation restrains their propagation because a higher (lower) local stress would be required to reach transformation stress. Depending on the overall temperature distribution, the nucleation of new phase fronts may be energetically more favorable than maintaining or increasing the propagation velocity of existing phase fronts. A higher strain rate means that the convective and conductive heat transport away from (to) the phase fronts does not keep pace

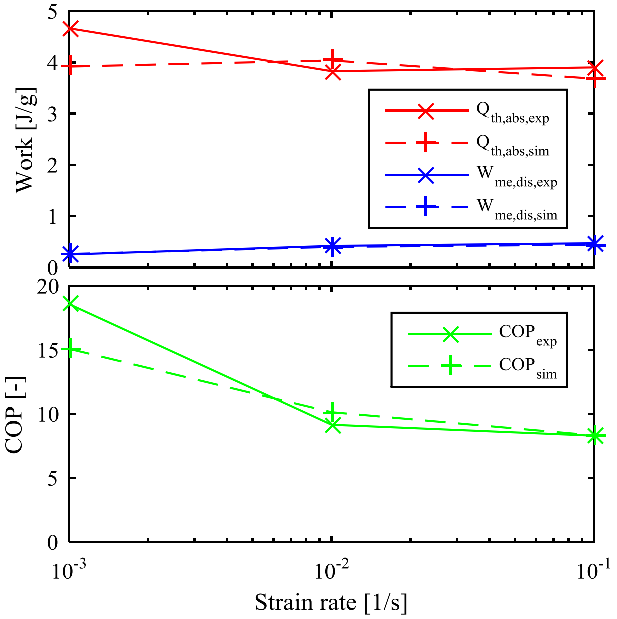

Fig. 10 Comparison of experiment and simulation for calculated dissipated mechanical work input and absorbed thermal energy output at different strain rates $\varepsilon' = 10^{-3} \dots 10^{-1}\,\mathrm{s}^{-1}$

with transformation-induced release (absorption) of latent heat resulting in higher (lower) local temperatures, which increase (decrease) transformation stress of the material.

The next to last row of Fig. 8 compares the calculated mechanical work using Eq. (3) for the different strain rates. Experiment (solid) and simulation (dotted) show that the work input during loading increases and the returned work during unloading decreases for higher strain rates. Therefore, the dissipated mechanical work in the cycle increases with the strain rate as shown in the upper part of Fig. 10 (blue). This behavior is well-known from the thermo-mechanical coupling in SMA material and reproduced correctly by the model. The thermal energy exchanged with the environment calculated by Eq. (6) is presented in the last row of Fig. 8. During loading and subsequent holding, the released latent heat is entirely transferred to the ambience while the sample reaches T_0 again. As the specimen transforms almost completely at this state as indicated by the joining temperature fronts, this thermal energy provides a good estimate of the latent heat in this material. A value of $5\,\mathrm{J/g}$, as listed in Table 1, results in a reasonable agreement of the thermal behavior between experiment and simulation.

The absorbed thermal energy is presented in the upper part of Fig. 10 (red). A nearly strain rate-independent value is expected since the amount of transformed material is similar for these experiments, because applied strain and ambient temperature are equal and the sample has sufficient time to exchange all latent heats. A deviation of less than 15% between experiment and simulation justifies the model simplification based on a one-dimensional single-crystal approach.

The lower part of Fig. 10 compares the computed COPs for different strain rates. The range of 8 to 19 matches typical values for elastocaloric cooling based on SMA [41]. As the absorbed thermal energy is approximately constant and the dissipated mechanical work increases with strain rate, the COP drops for higher (un)loading speeds. The simulation captures this characteristic and provides fairly accurate results, especially for higher strain rates, which will probably be used in cooling applications to achieve sufficient cooling power.

4 Conclusions

In this paper, we have presented a new model for the simulation of the uniaxial approximation for the localized transformation behavior of superelastic SMA thin films. The model is capable of reproducing distinctive phenomena observed in experiments during phase transformation induced by tensile deformation for strain rates over several orders of magnitude.

The material behavior was described using an extended version of the MAS model, which was originally designed to describe the thermo-mechanically coupled transformation behavior of SMA under the assumption of homogeneity. The model was extended by a localization effect induced by considering lateral contraction and transformation softening of the material. Furthermore, a non-local modification of the kinetic equations for phase transformation was included.

The simulation results for strain rates over three orders of magnitude were compared with the results from corresponding experiments. In both, the SMA sample was subject to a load/unload cycle with waiting periods to reach ambient temperature both after loading and unloading. Good agreement in mechanical and caloric data between experimental and numerical results was observed. Tensile force versus displacement diagrams showed not only the expected slopes, which increase with increasing strain rates but also the additional relaxation and contraction associated with continuing transformations after loading and unloading, respectively.

Comparison of the uniaxial, numerical temperature field with temperature data measured on the centerline of the film by IR thermography also shows a good quantitative prediction on the travel, the number and the temperature levels of the phase fronts. While very slow tensile deformation leads to only two phase fronts traveling along the film, at higher strain rates the transformation stress changes induced by temperature differences. In both experiment and simulation, this results in the propagation of phase fronts being restrained and new phase fronts being generated in preferred locations. However, a precise reproduction of the positions of the transformation bands cannot be expected as this is influenced by arbitrary material or setup imperfections.

Effects reproduced in the presented simulations greatly influence the efficiency of elastocaloric cooling devices. For cooling applications, the thermal behavior is also important. The presented model is able to predict the thermal energy exchange with the environment. The derived values as dissipated mechanical work and absorbed thermal work at the heat source are also accurately reproduced. This allows the calculation of the coefficient of performance for the elastocaloric cooling process. Careful design of a high-performance and efficient elastocaloric cooling process will therefore strongly benefit from the simulation model presented here.

Acknowledgements The authors gratefully acknowledge the support of the DFG priority program 1599 “Caloric effects in ferroic materials: New concepts for cooling” (www.ferroiccooling.de).

References

1. Fähler, S., Rößler, U.K., Kastner, O., Eckert, J., Eggeler, G., Emmerich, H., Entel, P., Müller, S., Quandt, E., Albe, K.: Caloric effects in ferroic materials: new concepts for cooling. Adv. Eng. Mater. **14**, 10–19 (2012)
2. Cui, J., Wu, Y., Muehlbauer, J., Hwang, Y., Radermacher, R., Fackler, S., Wuttig, M., Takeuchi, I.: Demonstration of high efficiency elastocaloric cooling with large Delta T using NiTi wires. Appl. Phys. Lett. **101**, 25–28 (2012)
3. Cui, J., Takeuchi, I., Wuttig, M., Wu, Y., Reinhard, R., Hwang, Y., Muehlbauer, J.: Thermoelastic cooling. http://www.google.com/patents/US20120273158 (2012)
4. Schmidt, M., Schütze, A., Seelecke, S.: Cooling efficiencies of a NiTi-based cooling process. In: ASME 2013 Conference on Smart Materials, Adaptive Structures and Intelligent Systems, p. V001T04A014 (2013)
5. Schmidt, M., Schütze, A., Seelecke, S.: Experimental investigation on the efficiency of a control dependent NiTi-based cooling process. In: ASME 2014 Conference on Smart Materials, Adaptive Structures and Intelligent Systems, pp. V002T04A013 (2014). doi:10.1115/SMASIS2014-7561
6. Schmidt, M., Schütze, A., Seelecke, S.: Scientific test setup for investigation of shape memory alloy based elastocaloric cooling processes. Int. J. Refrig. **54**, 88–97 (2015)
7. Ullrich, J., Schmidt, M., Schütze, A., Wieczorek, A., Frenzel, J., Eggeler, G., Seelecke, S.: Experimental investigation and numerical simulation of the mechanical and thermal behavior of a superelastic shape memory alloy beam during bending. In: ASME 2014 Conference on Smart Materials, Adaptive Structures and Intelligent Systems (2014) (**to appear**)
8. Ossmer, H., Chluba, C., Krevet, B., Quandt, E., Rohde, M., Kohl, M.: Elastocaloric cooling using shape memory alloy films. J. Phys. Conf. Ser. **476**, 12138 (2013)
9. Ossmer, H., Lambrecht, F., Gültig, M., Chluba, C., Quandt, E., Kohl, M.: Evolution of temperature profiles in TiNi films for elastocaloric cooling. Acta Mater. **81**, 9–20 (2014)
10. Ossmer, H., Chluba, C., Gueltig, M., Quandt, E., Kohl, M.: Local evolution of the elastocaloric effect in TiNi-based films. Shape Mem. Superelasticity **1**, 142–152 (2015)
11. Carmo, J.P., Silva, M.F., Ribeiro, J.F., Wolffenbuttel, R.F., Alpuim, P., Rocha, J.G., Gonçalves, L.M., Correia, J.H.: Digitally-controlled array of solid-state microcoolers for use in surgery. Microsyst. Technol. **17**, 1283–1291 (2011)
12. El-Ali, J., Perch-Nielsen, I.R., Poulsen, C.R., Bang, D.D., Telleman, P., Wolff, A.: Simulation and experimental validation of a SU-8 based PCR thermocycler chip with integrated heaters and temperature sensor. Sens. Actuators A Phys. **110**, 3–10 (2004)
13. Bechtold, C., Chluba, C., Lima De Miranda, R., Quandt, E.: High cyclic stability of the elastocaloric effect in sputtered TiNiCu shape memory films. Appl. Phys. Lett. **101**, 091903 (2012)
14. Chluba, C., Ge, W., Lima de Miranda, R., Strobel, J., Kienle, L., Quandt, E., Wuttig, M.: Ultralow-fatigue shape memory alloy films. Science **348**, 1004–1007 (2015)

15. Frenzel, J., Wieczorek, A., Opahle, I., Maaß, B., Drautz, R., Eggeler, G.: On the effect of alloy composition on martensite start temperatures and latent heats in Ni-Ti-based shape memory alloys. Acta Mater. **90**, 213–231 (2015)
16. Achenbach, M., Müller, I.: A model for shape memory. J. Phys. Colloq. **43**, C4-163–C4-167 (1982)
17. Achenbach, M.: A model for an alloy with shape memory. Int. J. Plast. **5**, 371–395 (1989)
18. Boyd, J.G., Lagoudas, D.C.: A thermodynamical constitutive model for shape memory materials. Part I. The monolithic shape memory alloy. Int. J. Plast. **12**, 805–842 (1996)
19. Brinson, L.C.C.: One-dimensional constitutive behavior of shape memory alloys: thermomechanical derivation with non-constant material functions and redefined martensite internal variable. J. Intell. Mater. Syst. Struct. **4**, 229–242 (1993)
20. Chemisky, Y., Duval, A., Patoor, E., Ben Zineb, T.: Constitutive model for shape memory alloys including phase transformation, martensitic reorientation and twins accommodation. Mech. Mater. **43**, 361–376 (2011)
21. Heintze, O., Seelecke, S.: A coupled thermomechanical model for shape memory alloys-from single crystal to polycrystal. Mater. Sci. Eng. A. **481–482**, 389–394 (2008)
22. Lagoudas, D.C.: Shape Memory Alloys. Springer, Boston (2010)
23. Seelecke, S., Müller, I.: Shape memory alloy actuators in smart structures: modeling and simulation. Appl. Mech. Rev. **57**, 23 (2004)
24. Seelecke, S.: Modeling the dynamic behavior of shape memory alloys. Int. J. Nonlinear Mech. **37**, 1363–1374 (2002)
25. Smith, R.C., Seelecke, S., Dapino, M., Ounaies, Z.: A unified framework for modeling hysteresis in ferroic materials. J. Mech. Phys. Solids. **54**, 46–85 (2006)
26. Shaw, J.A., Kyriakides, S.: Thermomechanical aspects of NiTi. J. Mech. Phys. Solids. **43**, 1243–1281 (1995)
27. Chang, B.-C., Shaw, J., Iadicola, M.: Thermodynamics of shape memory alloy wire: modeling, experiments, and application. Contin. Mech. Thermodyn. **18**, 83–118 (2006)
28. Duval, A., Haboussi, M., Ben Zineb, T.: Modelling of localization and propagation of phase transformation in superelastic SMA by a gradient nonlocal approach. Int. J. Solids Struct. **48**, 1879–1893 (2011)
29. Grandi, D., Maraldi, M., Molari, L.: A macroscale phase-field model for shape memory alloys with non-isothermal effects: influence of strain rate and environmental conditions on the mechanical response. Acta Mater. **60**, 179–191 (2012)
30. Depriester, D., Maynadier, A., Lavernhe-Taillard, K., Hubert, O.: Thermomechanical modelling of a NiTi SMA sample submitted to displacement-controlled tensile test. Int. J. Solids Struct **51**, 1901–1922 (2014)
31. Levitas, V.I., Lee, D.-W., Preston, D.L.: Interface propagation and microstructure evolution in phase field models of stress-induced martensitic phase transformations. Int. J. Plast. **26**, 395–422 (2010)
32. Furst, S.J., Crews, J.H., Seelecke, S.: Numerical and experimental analysis of inhomogeneities in SMA wires induced by thermal boundary conditions. Contin. Mech. Thermodyn. **24**, 485–504 (2012)
33. Richter, F., Kastner, O., Eggeler, G.: Implementation of the Müller–Achenbach–Seelecke model for shape memory alloys in ABAQUS. J. Mater. Eng. Perform. **18**, 626–630 (2009)
34. Yang, S., Seelecke, S.: FE analysis of SMA-based bio-inspired bone–joint system. Smart Mater. Struct. **18**, 104020 (2009)
35. Müller, I., Seelecke, S.: Thermodynamic aspects of shape memory alloys. Math. Comput. Model. **34**, 1307–1355 (2001)
36. Young, M.L., Wagner, M.F.X., Frenzel, J., Schmahl, W.W., Eggeler, G.: Phase volume fractions and strain measurements in an ultrafine-grained NiTi shape-memory alloy during tensile loading. Acta Mater. **58**, 2344–2354 (2010)
37. COMSOL AB: COMSOL Multiphysics, User's Guide, Version 5.1 (2015)
38. Brinson, L.C., Schmidt, I., Lammering, R.: Stress-induced transformation behavior of a polycrystalline NiTi shape memory alloy: Micro and macromechanical investigations via in situ optical microscopy. J. Mech. Phys. Solids. **52**, 1549–1571 (2004)
39. Khalil-Allafi, J., Hasse, B., Klönne, M., Wagner, M., Pirling, T., Predki, W., Schmahl, W.W.: In-situ diffraction investigation of superelastic NiTi shape memory alloys under mechanical stress with neutrons and with synchrotron radiation. Materwiss. Werksttech. **35**, 280–283 (2004)
40. Schmahl, W.W., Khalil-Allafi, J., Hasse, B., Wagner, M., Heckmann, a, Somsen, C.: Investigation of the phase evolution in a super-elastic NiTi shape memory alloy (50.7 at.%Ni) under extensional load with synchrotron radiation. Mater. Sci. Eng. A. **378**, 81–85 (2004)
41. Schmidt, M., Schütze, A., Seelecke, S.: Elastocaloric cooling processes: the influence of material strain and strain rate on efficiency and temperature span. APL Mater. **4**, 0-6 (2016)